Check for updates

Sonochemistry-enabled uniform coupling of SnO$_2$ nanocrystals with graphene sheets as anode materials for lithium–ion batteries†

Xiaoyan Han, [ID] [a] Ran Li, [b] Shengqiang Qiu, [b] Xiaofang Zhang, [a] Qing Zhang*[ac] and Yingkui Yang [ID] [abc]

SnO$_2$/graphene nanocomposite was successfully synthesized by a facile sonochemical method from SnCl$_2$ and graphene oxide (GO) precursors. In the sonochemical process, the Sn^{2+} is firstly dispersed homogeneously on the GO surface, then *in situ* oxidized to SnO$_2$ nanoparticles on both sides of the graphene nanosheets (RGO) obtained by the reduction of GO under continuous ultrasonication. Graphene not only provides a mechanical support to alleviate the volume changes of the SnO$_2$ anode and prevent nanoparticle agglomeration, but also serves as a conductive network to facilitate charge transfer and Li$^+$ diffusion. When used as a lithium ion battery (LIB) anode, the SnO$_2$/graphene nanocomposite exhibits significantly improved specific capacity (1610 mA h g^{-1} at 100 mA g^{-1}), good cycling stability (retaining 87% after 100 cycles), and competitive rate performance (273 mA h g^{-1} at 500 mA g^{-1}) compared to those of bare SnO$_2$. This sonochemical method can be also applied to the synthesis of other metal-oxide/graphene composites and this work provides a large-scale preparation route for the practical application of SnO$_2$ in lithium ion batteries.

Introduction

Lithium ion batteries (LIBs) have been intensively used in portable electronics, electric vehicles (EVs), and intelligent power grids due to their superior advantages such as long cycle life, high energy density, environmental friendliness and no memory effect.[1–4] Electrode materials play a critical role on electrochemical performance of LIBs. Among various anode materials, transition-metal oxides have been widely investigated for their abundant resources and high specific capacity. Unfortunately, they all endure dramatic volume change during the lithiation/delithiation process, resulting in pulverization and flaking off of active materials, thus leading to rapid capacity decay.[5,6] Among various transition metal oxides, SnO$_2$ is considered as one of the most promising electrode material due to its high theoretical capacity (782 mA h g^{-1}), low discharge potential (<1.5 V), environmental benignity and low-cost.[7–9] However, the electrochemical performance of bare SnO$_2$ is unsatisfactory for large volume change (∼300%), low electronic conductivity, and poor transport kinetics.[10–13]

To alleviate volume change during lithiation/delithiation process and enhance structural stability of SnO$_2$, an effective strategy is to design nanostructured SnO$_2$.[14–17] However, the agglomeration of nanostructured SnO$_2$ during the cycling process usually leads to fast capacity attenuation.[18,19] Recently, nanocomposites have drawn wide attention for their superiorities to integrate multiple properties of different nanoscale building blocks to improve mechanical and electronic properties.[20–24] Particularly, graphene-based nanocomposites with metal, metal oxides or polymers have also demonstrated particular mechanical, electronic, electrochemical and catalytic properties.[25–28] Hence, various SnO$_2$/graphene nanocomposites with enhanced electrochemical performance have been fabricated, in which graphene supplies a mechanical support to prevent volume changes and enhances electrical conductivity of composites.[29–31] In addition, flexible graphene support with high surface area, porosity, electrical conductivity and chemical inertness can prevent nanoparticle agglomeration to achieve a stable electrode structure and provide good electric conductivity for the composite.[32–34]

Various methods have been used to prepare SnO$_2$/graphene nanocomposites and each method has its own merits and demerits. For example, Lee *et al.* prepared SnO$_2$/3D graphene hybrid material by a simple hydrothermal process,[35] Wang and co-workers developed a ternary self-assembly approach to construct layered SnO$_2$-graphene nanocomposites,[36] and

[a]Key Laboratory of Resources Green Conversion and Utilization of State Ethnic Affairs Commission & Ministry of Education, South-Central University for Nationalities, Wuhan 430074, China. E-mail: qingzhang@mail.scuec.edu.cn

[b]School of Materials Science and Engineering, Hubei University, Wuhan 430062, China

[c]Hubei Engineering Technology Research Centre for Energy Polymer Materials, School of Chemistry and Materials Science, South-Central University for Nationalities, Wuhan 430074, China

† Electronic supplementary information (ESI) available. See DOI: 10.1039/c9ra00554d

Zhang's group synthesized SnO$_2$@graphene nanocomposites *via* a wet mechanochemical method.[37] Compared to these reported methods, sonochemical methods are more favorable for the construction of nanostructures without involving any surfactants and complex processes, and the morphology and particle size can be regulated by ultrasonic waves.[38–41] In fact, the basic principle of sonochemistry method is the acoustic cavitation phenomenon in a liquid, which arises high temperature and pressure, and high cooling rate instantaneously during the cavitation process.[38,41] Such extreme conditions can trigger the formation of metal oxides on a nanometer scale with homogeneous particle size distribution.[42–45] Herein, SnO$_2$/graphene nanocomposite (SnO$_2$/RGO) was synthesized *via* a simple and effective sonochemical method using SnCl$_2$ and graphene oxide (GO) as precursors. When used as a LIBs anode, the as-prepared SnO$_2$/RGO nanocomposite displays large specific capacity (1610 mA h g^{-1} at 100 mA g^{-1}), good cycling performance (87% retention after 100 cycles) and competitive rate capability (273 mA h g^{-1} at 500 mA g^{-1}).

Experimental

Synthesis of SnO$_2$/RGO nanocomposite

Graphene oxide (GO) was prepared from graphite powders (>95%) according to a modified Hummer's method.[46] SnO$_2$/graphene nanocomposite was synthesized by a sonochemical method using SnCl$_2$ and GO as precursors. Firstly, ethanol aqueous solution (1 : 1 mol) and SnCl$_2$ (1‰ mol) were added into the GO aqueous solution under vigorous stirring to obtain uniform mixture. After stirring for 30 min, the mixture was then transferred into a wrapped beaker by ultrasonic irradiation at 50 °C for 3 h under ultrasonic power of 400 W in a bath sonicator. The resulting dark-grey precipitate was collected by centrifugation, washed and then dried at 80 °C under vacuum overnight. Finally, the product was heated at 550 °C for 3 h in argon gas with a heating rate of 5 °C min^{-1}. The resulting products with 0 wt% and 30 wt% of GO were marked as bare SnO$_2$ and SnO$_2$/RGO nanocomposite, respectively. RGO was obtained from GO by the same heat treatment conditions.

In this work, a sonochemical method was employed to synthesize SnO$_2$/RGO nanocomposite by using SnCl$_2$ as reducing agent and graphene oxide (GO) as oxidizing agent. The possible reaction mechanism is proposed according to the following equations:[37]

$$SnCl_2 + H_2O \leftrightarrow Sn(OH)Cl + HCl \tag{1}$$

$$Sn(OH)Cl + GO \rightarrow SnO_2/graphene + HCl \tag{2}$$
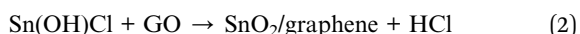
In the sonochemical reaction, SnCl$_2$ is firstly hydrolyzed to Sn(OH)Cl as shown in reaction (1), subsequently Sn(OH)Cl is oxidized to SnO$_2$ and GO is reduced to graphene (RGO) under continuous ultrasonic forces. As shown in Fig. 1, Sn(OH)Cl can be dispersed homogeneously on the surface of two-dimensional graphene nanosheets in ethanol solution under constant ultrasonication. The ultrasound treatment triggers the redox
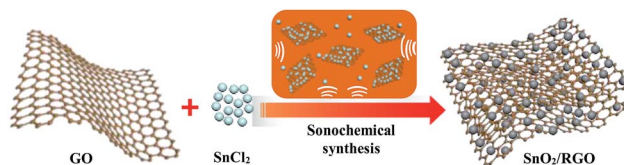

Fig. 1 Illustration of sonochemical method synthesis process of SnO$_2$/RGO.

reaction between SnCl$_2$ and GO, and *in situ* synthesis of SnO$_2$ nanoparticles onto the graphene surface.

Measurements

X-ray diffraction (XRD) were performed on a Bruker D8-advance diffractometer with a Ni filter and Cu Kα radiation. Scanning electron microscopy (SEM) was observed by using a Hitachi SU8010 microscope. Transmission electron microscopy (TEM) was implemented by a Tecnai G2 20 S-TWIN microscopy at 200 kV. Fourier transform infrared spectroscopy (FT-IR) spectra were recorded on a Nicolet AVATAR-360 spectrometer. Raman spectra were performed on a DXR Raman microscope excited (Thermo Scientific) by 514 nm. Thermogravimetric analysis (TGA) curves were taken on a thermogravimetric analyzer (NETZSCH, TG209F3) from 40 to 800 °C at 20 °C min^{-1} in air atmosphere. X-ray photoelectron spectroscopy (XPS) spectra of the samples were recorded on a Thermo MultiLab 2000 X-ray photoelectron spectrometer.

The electrochemical performance was carried out using a 2032-type coin cells (CR2032). A lithium foil was used as the counter electrode and a Celgard-2400 microporous membrane was used as the separator. The working electrode consists of 80 wt% active material, 10 wt% acetylene black and 10 wt% polyvinylidene fluoride (PVDF) binder. A copper foil acted as the current collector. 1.0 M LiPF$_6$ solution dissolved in ethylene carbonate (EC) and dimethylcarbonate (DMC) (1 : 1, v/v) was used as the electrolyte. The cells were assembled in an argon-filled glove box. The galvanostatic discharge/charge tests were studied between 0.001 and 2.0 V *versus* Li$^+$/Li on a multichannel battery testing system (LAND CT2001A). Cyclic voltammetry (CV) experiments and electrochemical impedance spectroscopy (EIS) were performed on an electrochemical working station (CHI770E) using model cells. CV were recorded at scan rate of 0.2 mV s^{-1} in the potential range of 0.001–2.0 V. EIS was examined in a frequency range from 0.01 Hz to 100 kHz under AC amplitude of 5 mV.

Results and discussion

The morphology and microstructure were elucidated by SEM and TEM. Fig. 2a shows distinct lamellar structure of GO sheets, which contains a few layers. Bare SnO$_2$ consists of mono-dispersed nanoparticles with an average particle size of about 10 nm, which shows obviously agglomeration (Fig. 2b). In contrast, SnO$_2$ nanoparticles are well adhered on the surface of RGO nanosheets in the nanocomposite as shown in Fig. 2c and d. Due to the electrostatic interaction between SnO$_2$ and residual oxygen-containing groups in RGO, the sonochemical
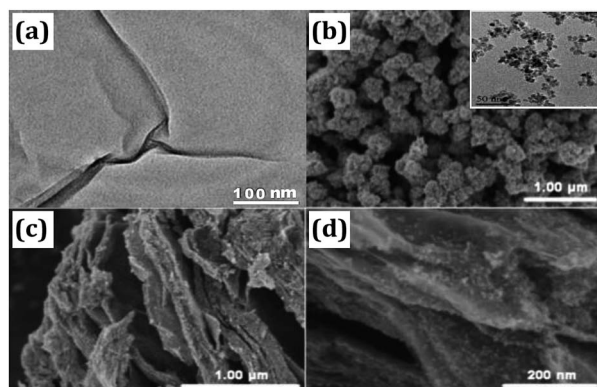
Fig. 2 (a) TEM image of GO. (b) SEM image of bare SnO_2. (c and d) SEM images of SnO_2/RGO. The inset in (b) shows a TEM image of bare SnO_2.

process can effectively inhibit the aggregation of SnO_2 nanoparticles and realize the uniform distribution of SnO_2 on the surface of RGO sheets.

XRD patterns of GO, bare SnO_2 and SnO_2/RGO are given in Fig. 3. GO displays only one broad peak located at 10.8°, indexing to the (001) plane of GO with an interlayer distance of 8.18 Å.[47] Bare SnO_2 and SnO_2/RGO exhibit similar diffraction peaks, which are well indexed to the pure SnO_2 (JCPDS no. 41-1445), indicating that the reduction of GO does not affect the crystal structure of SnO_2. However, the typical stacking peak of graphene nanosheets located at 26° is also absent in the pattern of SnO_2/RGO nanocomposite. This indicates that SnO_2 particles are formed on the both sides of RGO nanosheets, which prevents graphene sheets from restacking.[48] In addition, compared to sharp diffraction peaks of SnO_2, SnO_2/RGO nanocomposite displays broader XRD peaks, which is attributed to the decrease of particle size (bare SnO_2: 10.8 nm, SnO_2/RGO: 7.8 nm, calculated by Scherrer formula: $D = K\lambda/B \cos \theta$), suggesting that the growth of SnO_2 nanoparticles on the surface of RGO nanosheets can prevent nanoparticles agglomeration. Furthermore, no other peaks can be observed, indicating the complete transformation of $SnCl_2$ into SnO_2 upon sonochemical and heat treatment process.
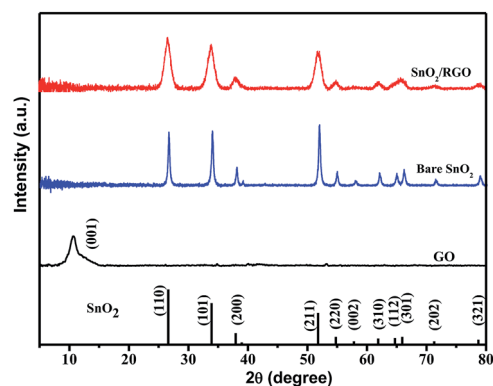
Fig. 4a shows FT-IR spectra of bare SnO_2, GO and SnO_2/RGO. FT-IR spectrum of GO is in good agreement with previous works.[49] GO shows the O–H deformation peak at 1401 cm^{-1}, the O–H stretching vibrations peak at 3420 cm^{-1} and the C=O stretching vibrations peak at 1735 cm^{-1}. The peaks at 1624, 1220, and 1052 cm^{-1} are due to C=C bending vibrations, C–OH stretching vibrations, and C–O stretching vibrations, respectively. Those peaks weaken or almost disappear for the SnO_2/RGO nanocomposite, implying that GO is completely reduced to RGO nanosheets during the formation of nanocomposite. Additionally, a strong peak at 624 cm^{-1} is assigned to Sn–O stretching vibrations, confirming the presence of SnO_2 in the composite.[48,49] The FT-IR results confirm the reduction of GO and the oxidation of Sn^{2+} to SnO_2, suggesting the formation of SnO_2/RGO nanocomposite.
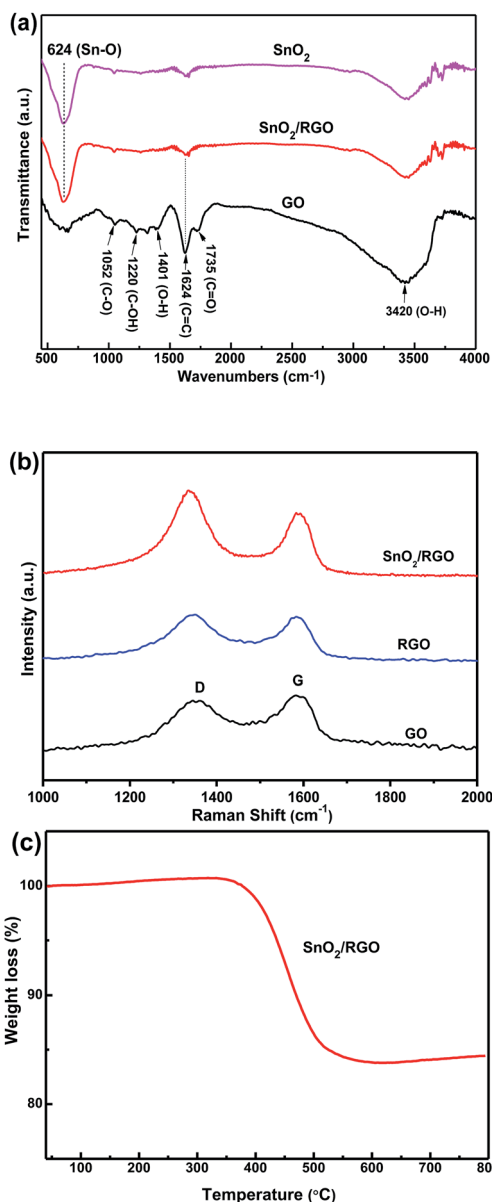

Fig. 4 (a) FT-IR of GO, bare SnO_2, and SnO_2/RGO nanocomposite. (b) Raman spectra of GO, RGO, and SnO_2/RGO nanocomposite. (c) TGA curve of SnO_2/RGO nanocomposite in air atmosphere.

Fig. 3 XRD patterns of GO, bare SnO_2 and SnO_2/RGO nanocomposite.

Fig. 4b gives Raman spectra of GO, RGO and SnO_2/RGO. The peaks at 1588 and 1344 cm^{-1} correspond to the G and D band, respectively. The G band is related to the presence of isolated double bonds in a 2-dimensional hexagonal lattice, while the D band is linked with the defects and disorder in the hexagonal graphitic layers. The relative intensity ratio of D to G bands (I_D/I_G) can represent the reduction degree of carbonaceous materials. The defect density is calculated to be 2.0 for SnO_2/RGO nanocomposite, larger than that of GO (0.9) and RGO (1.0). This enhancement of defect density could be ascribed to the exfoliation and reduction of GO with the attachment of SnO_2 nanoparticles on the surface.[50]

To obtain the content of RGO in the composite, thermogravimetric analysis (TGA) was measured under air as shown in Fig. 4c. In general, the negligible weight loss below 400 °C is attributed to adsorbed water molecules and oxygen-containing groups of graphene in the sample. The significant weight loss between 400 and 600 °C is attributed to the complete combustion of carbon components from RGO. Above 600 °C, the weight of the sample is constant, indicating that the combustion is completed and only SnO_2 is left. The weight loss of SnO_2/RGO nanocomposite is 18.2% (RGO component), which is different from pre-designed feed ratio of GO (30%). This deviation can be ascribed to the loss of oxygen-containing groups in GO during thermal reduction process.

XPS was further employed to confirm the reduction of GO and formation of SnO_2 during the sonochemical process. Fig. 5a shows the survey spectra of GO, bare SnO_2 and SnO_2/RGO. The spectrum of GO only shows two distinguishable peaks of carbon (C 1s, 285 eV) and oxygen (O 1s, 530 eV). In contrast, the spectrum of SnO_2/RGO shows all the peaks of desired carbon, oxygen and SnO_2. The Sn 3d peaks of SnO_2/RGO (Fig. 5b) could be resolved into 487.0 and 495.4 eV with an 8.4 eV peak-to-peak separation, corresponding to Sn $3d_{5/2}$ and Sn $3d_{3/2}$, respectively, which are consistent with the previous reports about SnO_2/C composites.[48,51] Additionally, the peaks of C 1s spectra of SnO_2/RGO and GO could be resolved into four binding energies (Fig. 5c and d), corresponding to four types of carbon atoms (C–C/C=C: 284.7 eV, C–O: 286.7 eV, C=O: 288.7 eV, and O–C=O: 289.6 eV).

The C–C/C=C content in SnO_2/RGO (77.8%) is larger than that of GO (36.7%). Meanwhile, C–O amount in SnO_2/RGO declines sharply due to successful removal of oxygen-containing groups in GO, which further confirms the completely reduction of GO.

Fig. 6a shows CV curves of SnO_2/RGO for the first three cycles. It has been established that two-step reactions are involved in the SnO_2-based electrodes:

$$SnO_2 + 4Li^+ + 4e^- \rightarrow Sn + 2Li_2O \tag{3}$$

$$Sn + xLi^+ + xe^- \leftrightarrow Li_xSn \ (0 \leq x \leq 4.4) \tag{4}$$
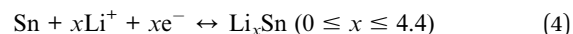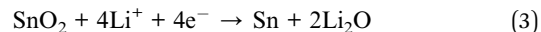
There is an obvious cathodic peak at 0.72 V in the first cycle of the SnO_2/RGO, which is attributed to the reduction of SnO_2 to metallic Sn and formation of amorphous Li_2O as indicated in reaction (3) as well as the formation of solid electrolyte interphase (SEI).[31,50] The broad cathodic peak at about 0.25 V and anodic peak at about 0.65 V correspond to reversible reaction as indicated in reaction (4). The anodic peak at about 1.32 V represents partial reversibility of the reaction as shown in reaction (3).[31] The CV curves of the second and third cycles are almost overlapped, implying an excellent cycling stability and reversibility of the SnO_2/RGO. Furthermore, charge/discharge profiles of the SnO_2/RGO are displayed in Fig. 6b. There appears two discharge plateaus around 0.8 V and 0.3 V in the first discharge process, originating from the formation of SEI film and alloying of Li_xSn. A charge plateau at 1.2 V in the first cycle is linked with dealloying of Li_xSn,[13] which is consistent with the oxidation–reduction peaks of CV curves. The initial discharge and charge capacities of the SnO_2/RGO electrode are 1610 and 765 mA h g^{-1}, respectively. This large initial irreversible loss (52%) is common for SnO_2 materials, which could be assigned to the irreversible transformation reaction as described in eqn (3) and the formation of solid electrolyte interphase (SEI) film.

Fig. 6c compares the cycling performances of SnO_2/RGO with bare SnO_2 and RGO. Apparently, bare RGO shows good cycling
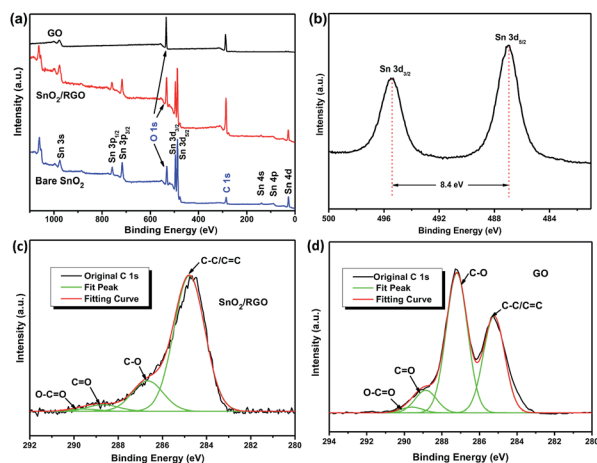
Fig. 5 (a) XPS spectra of GO, bare SnO_2 and SnO_2/RGO. (b) Sn 3d XPS spectra of SnO_2/RGO. C 1s XPS spectra of (c) SnO_2/RGO and (d) of GO.
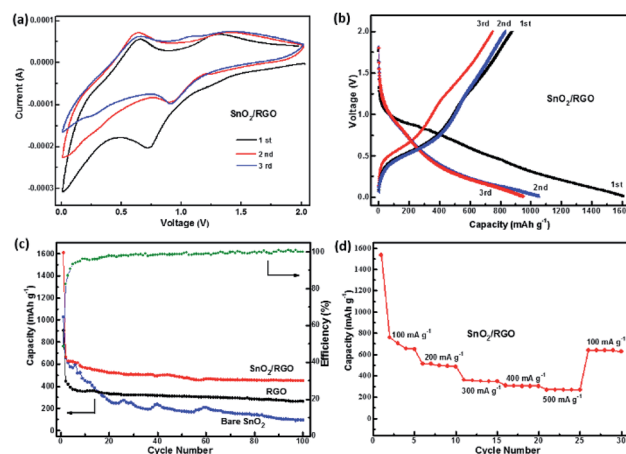
Fig. 6 (a) CV curves of the SnO_2/RGO at 0.2 mV s^{-1}. (b) Charge/discharge voltage profiles of the SnO_2/RGO at a current density of 100 mA g^{-1}. (c) Cycling performance and coulombic efficiency of the bare SnO_2, RGO and SnO_2/RGO at 100 mA g^{-1}. (d) The rate performance of SnO_2/RGO.

stability but low reversible capacity. After 100 cycles, the discharge capacity decreases to 263 mA h g^{-1}. Even though bare SnO$_2$ delivers a high discharge capacity (1024 mA h g^{-1}), but the capacity tends to decay quickly to below 95 mA h g^{-1} after 100 cycles. In contrast, the cycling performance of SnO$_2$/RGO electrode is substantially improved. Although there is still some capacity decay within the initial 20 cycles, the capacity of SnO$_2$/RGO tends to level off in following cycles. It is important to note that SnO$_2$/RGO delivers initial discharge capacity as high as 1610 mA h g^{-1} and a reversible capacity of 450 mA h g^{-1} can be retained over 100 cycles (C_{100th}/C_{20th} = 87%) with the coulombic efficiency of 100%. These results indicate that SnO$_2$/RGO shows improved cycling stability and higher reversible capacity than bare SnO$_2$. Moreover, to fully estimate the electrochemical performance of SnO$_2$/RGO electrode, the rate performance at current densities of 100, 200, 300, 400 and 500 mA g^{-1} are also shown in Fig. 6d. As the current density increases from 100 to 500 mA g^{-1}, the reversible capacity varies from 650 to 512, 360, 311 and 273 mA h g^{-1}, respectively. Additionally, when the current density returns to 100 mA g^{-1}, a reversible capacity of 639 mA h g^{-1} is recovered, thus demonstrating a competitive rate capability compared to the previously reported SnO$_2$-based composites as shown in Table S1.†[52–55] The above results show that the introducing of graphene nanosheets combines the respective advantages of SnO$_2$ and RGO, thus greatly enhances the overall electrochemical capacity and cycling stability of the SnO$_2$/RGO. In order to investigate the influence of GO content on the electrochemical performance of the composite, we also synthesized a series of SnO$_2$/RGO nanocomposites with various component ratios *via* regulating the feeding ratios of GO and SnCl$_2$ in the sonochemical reaction systems as shown in Fig. S1.† Considering that large amounts of graphene would in turn inevitably reduce the energy density of finished batteries, thus SnO$_2$/RGO (30 wt%) is considered to exhibit the best comprehensively electrochemical performance.

EIS measurements were performed for the bare SnO$_2$, RGO, and SnO$_2$/RGO electrode to further elucidate the influence of graphene nanosheets on the electrochemical behavior of the composite (Fig. 7). The inset is the equivalent circuit used for fitting the impedance spectrum. R_s represents the ohmic resistance from the system and C_d is the double-layer capacity.[28] In the Nyquist plots, a semicircle in higher frequency region and an inclined line of approximately 45° slope at lower frequency region were observed for all materials. The semicircle can be ascribed to charge transfer resistance (R_{ct}) at the interface between the electrolyte and electrode, while the inclined line corresponds to Li$^+$ diffusion process in the bulk of the electrode and represents the Warburg impedance (W).[48] The values of R_{ct} for the bare SnO$_2$, RGO and SnO$_2$/RGO are calculated to be 1088, 597, and 464 Ω, respectively. Apparently, SnO$_2$/RGO shows smaller R_{ct} than that of bare SnO$_2$, which is ascribed to the enhanced electronic conductivity provided by the graphene substrate. Moreover, the high slope of inclined line for SnO$_2$/RGO is a characteristic of low Z_w, suggesting fast Li$^+$ diffusion in the composite electrode. The results confirm that the presence of graphene nanosheets indeed facilitates charge transfer and Li$^+$ diffusion during the electrochemical lithiation/delithiation process, which accounts for the enhanced electrochemical performance.

Conclusions

In conclusion, a facile sonochemical method has been developed to synthesize SnO$_2$/RGO nanocomposite by *in situ* oxidizing SnCl$_2$ to SnO$_2$ and reducing GO to RGO. The individual dispersed SnO$_2$ nanoparticles are fully well-adhered on the both sides of graphene nanosheets. This unique structure results in high specific surface area, stable framework, and remarkable electron and ion transport, thereby resulting in a superior electrochemical performance. When used as LIBs anode, SnO$_2$/RGO delivers initial discharge specific capacity as high as about 1610 mA h g^{-1}, with the initial coulombic efficiency of about 48%. Moreover, the SnO$_2$/RGO electrode shows good cycling stability, about 87% of the capacity is maintained (C_{100th}/C_{20th}) after 100 cycles at 100 mA g^{-1}. Additionally, the SnO$_2$/RGO electrode shows a competitive rate performance. A capacity of 273 mA h g^{-1} can be retained at a high current density up to 500 mA g^{-1}, and 639 mA h g^{-1} can still be recovered once the current density is returned to 100 mA g^{-1}. This facile sonochemical method can be also applied to the synthesis of other graphene/metal-oxide composites and this work provides a large-scale preparation route for the practical application of SnO$_2$ in lithium ion batteries.

Conflicts of interest

There are no conflicts to declare.

Acknowledgements

Fig. 7 EIS tests with Nyquist plots and equivalent circuit of the bare SnO$_2$, RGO and SnO$_2$/RGO.

Notes and references

1 J.-M. Tarascon and M. Armand, *Nature*, 2001, **414**, 359.
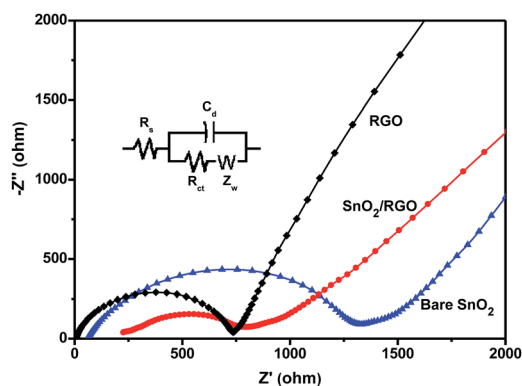2 Y. G. Guo, J. S. Hu and L. J. Wan, *Adv. Mater.*, 2008, **20**, 2878.

3 J. B. Goodenough and K. S. Park, *J. Am. Chem. Soc.*, 2013, **135**, 1167.

4 D. B. Xiong, X. F. Li, Z. M. Bai and S. G. Lu, *Small*, 2018, **14**, 1703419.

5 D. Zhou, W. L. Song, X. G. Li and L. Z. Fan, *Electrochim. Acta*, 2016, **207**, 9.

6 Q. H. Tian, Y. Tian, Z. X. Zhang, L. Yang and S. Hirano, *J. Power Sources*, 2015, **280**, 397.

7 D. N. Wang, J. L. Yang, X. F. Li, D. S. Geng, R. Y. Li, M. Cai, T. K. Sham and X. L. Sun, *Energy Environ. Sci.*, 2013, **6**, 2900.

8 K. Kravchyk, L. Protesescu, M. I. Bodnarchuk, F. Krumeich, M. Yarema, M. Walter, C. Guntlin and M. V. Kovalenko, *J. Am. Chem. Soc.*, 2013, **135**, 4199.

9 J. Liang, X. Y. Yu, H. Zhou, H. B. Wu, S. J. Ding and X. W. Lou, *Angew. Chem., Int. Ed.*, 2014, **53**, 12803.

10 L. Zhang, G. Zhang, H. B. Wu, L. Yu and X. W. Lou, *Adv. Mater.*, 2013, **25**, 2589.

11 C. Guan, X. H. Wang, Q. Zhang, Z. X. Fan, H. Zhang and H. J. Fan, *Nano Lett.*, 2014, **14**, 4852.

12 H. K. Wang, J. K. Wang, D. X. Cao, H. Y. Gu, B. B. Li, X. Lu, X. G. Han, A. L. Rogach and C. M. Niu, *J. Mater. Chem. A*, 2017, **5**, 6817.

13 H. Y. Zhang, L. Q. Li, Z. P. Li, W. H. Zhong, H. Y. Liao and Z. H. Li, *Appl. Surf. Sci.*, 2018, **442**, 65.

14 J. P. Liu, Y. Y. Li, X. T. Huang, R. M. Ding, Y. Y. Hu, J. Jiang and L. Liao, *J. Mater. Chem.*, 2009, **19**, 1859.

15 X. M. Yin, C. C. Li, M. Zhang, Q. Y. Hao, S. Liu, L. B. Chen and T. H. Wang, *J. Phys. Chem. C*, 2010, **114**, 8084.

16 Z. X. Chen, M. Zhou, Y. L. Cao, X. P. Ai, H. X. Yang and J. Liu, *Adv. Energy Mater.*, 2012, **2**, 95.

17 W. J. Dong, J. J. Xu, C. Wang, Y. Lu, X. Y. Liu, X. Wang, X. T. Yuan, Z. Wang, T. Q. Lin, M. L. Sui, I. W. Chen and F. Q. Huang, *Adv. Mater.*, 2017, **29**, 1700136.

18 J. J. Liang, C. C. Yuan, H. H. Li, K. Fan, Z. X. Wei, H. Q. Sun and J. M. Ma, *Nano-Micro Lett.*, 2018, **10**, 21.

19 B. Huang, X. H. Li, Y. Pei, S. Li, X. Cao, R. C. Massé and G. Z. Cao, *Small*, 2016, **12**, 1945.

20 Y. F. Lu, Y. Yang, A. Sellinger, M. C. Lu, J. M. Huang, H. Y. Fan, R. Haddad, G. Lopez, A. R. Burns, D. Y. Sasaki, J. Shelnutt and C. J. Brinker, *Nature*, 2001, **410**, 913.

21 H. Zeng, J. Li, J. P. Liu, Z. L. Wang and S. H. Sun, *Nature*, 2002, **420**, 395.

22 X. F. Zhang, H. Li, W. Zhang, Z. J. Huang, C. P. Tsui, C. H. Lu, C. E. He and Y. K. Yang, *Electrochim. Acta*, 2019, **301**, 55.

23 S. Lei, Y. Lu, X. F. Zhang, P. Y. Gao, X. Cui and Y. K. Yang, *Chem. Commun.*, 2019, DOI: 10.1039/C8CC10186H.

24 R. Li, X. L. Dong, C. E. He, Z. X. Liu, L. P. Huang and Y. K. Yang, *Int. J. Electrochem. Sci.*, 2017, **12**, 144.

25 X. S. Song, X. F. Li, Z. M. Bai, B. Yan, D. B. Xiong, L. X. Lin, H. Zhao, D. J. Li and Y. Y. Shao, *Carbon*, 2018, **133**, 14.

26 L. L. Fan, X. F. Li, X. S. Song, N. N. Hu, D. B. Xiong, A. Koo and X. L. Sun, *ACS Appl. Mater. Interfaces*, 2018, **10**, 2637.

27 M. Sahoo and S. Ramaprabhu, *Carbon*, 2018, **127**, 627.

28 C. E. He, Y. C. Liang, P. Y. Gao, L. Cheng, D. A. Shi, X. L. Xie, R. K. Y. Li and Y. K. Yang, *Composites, Part B*, 2017, **121**, 68.

29 S. M. Paek, E. J. Yoo and I. Honma, *Nano Lett.*, 2009, **9**, 72.

30 J. X. Guo, B. Jiang, X. Zhang and H. T. Liu, *J. Power Sources*, 2014, **262**, 15.

31 Q. X. Xie, Y. T. Zhu, P. Zhao, Y. F. Zhang and S. H. Wu, *J. Mater. Sci.*, 2018, **53**, 9206.

32 X. D Huang, X. F. Zhou, L. Zhou, K. Qian, Y. H Wang, Z. P. Liu and C. Z. Yu, *ChemPhysChem*, 2011, **12**, 278.

33 X. F. Li, X. B. Meng, J. Liu, D. S. Geng, Y. Zhang, M. N. Banis, Y. L. Li, J. L. Yang, R. Y. Li, X. L. Sun, M. Cai and M. W. Verbrugge, *Adv. Funct. Mater.*, 2012, **22**, 1647.

34 X. F. Zhou, W. J. Liu, X. Y. Yu, Y. J. Liu, Y. P. Fang, S. Klankowski, Y. Q. Yang, J. E. Brown and J. Li, *ACS Appl. Mater. Interfaces*, 2014, **6**, 7434.

35 J. I. Lee, J. H. Song, Y. Cha, S. F. Fu, C. Z. Zhu, X. L. Li, Y. H. Lin and M. K. Song, *Nano Res.*, 2017, **10**, 4398.

36 D. H. Wang, R. Kou, D. Choi, Z. G. Yang, Z. M. Nie, J. Li, L. V. Saraf, D. H. Hu, J. G. Zhang, G. L. Graff, J. Liu, M. A. Pope and I. A. Aksay, *ACS Nano*, 2010, **3**, 1587.

37 S. Li, Y. Z. Wang, C. Lai, J. X. Qiu, M. Ling, W. Martens, H. J. Zhao and S. Q. Zhang, *J. Mater. Chem. A*, 2014, **2**, 10211.

38 J. J. Zhu, Z. H. Lu, S. T. Aruna, D. Aurbach and A. Gedanken, *Chem. Mater.*, 2000, **12**, 2557.

39 K. G. Lee, J. M. Jeong, S. J. Lee, B. Yeom, M. K. Lee and B. G. Choi, *Ultrason. Sonochem.*, 2015, **22**, 422.

40 H. ullah, I. Khan, Z. H. Yamani and A. Qurashi, *Ultrason. Sonochem.*, 2017, **34**, 484.

41 V. S. Nalajala and V. S. Moholkar, *Ultrason. Sonochem.*, 2011, **18**, 345.

42 K. S. Suslick, S. B. Choe, A. A. Cichowlas and M. W. Grinstaff, *Nature*, 1991, **353**, 414.

43 K. Krishnamoorthy, G. S. Kim and S. K. Kim, *Ultrason. Sonochem.*, 2013, **20**, 644.

44 A. Abulizi, G. H. Yang and J. J. Zhu, *Ultrason. Sonochem.*, 2014, **21**, 129.

45 N. Duraisamy, A. Numan, S. Omar Fatin, K. Ramesh and S. Ramesh, *J. Colloid Interface Sci.*, 2016, **471**, 136.

46 W. S. Hummers and R. E. Offeman, *J. Am. Chem. Soc.*, 1958, **80**, 1339.

47 H. Malas and C. K. Das, *Composites, Part B*, 2015, **79**, 639.

48 S. Yang, W. B. Yue, J. Zhu, Y. Ren and X. J. Yang, *Adv. Funct. Mater.*, 2013, **23**, 3570.

49 Y. M. Li, X. J. Lv, J. Lu and J. H. Li, *J. Phys. Chem. C*, 2010, **114**, 21770.

50 M. Zhang, D. N. Lei, Z. F. Du, X. M. Yin, L. B. Chen, Q. H. Li, Y. G. Wang and T. H. Wang, *J. Mater. Chem.*, 2011, **21**, 1673.

51 G. M. An, N. Na, X. R. Zhang, Z. J. Miao, S. D. Miao, K. L. Ding and Z. M. Liu, *Nanotechnology*, 2007, **18**, 435707.

52 M. Sahoo and S. Ramaprabhu, *RSC Adv.*, 2017, **7**, 13789.

53 C. Zhu, D. H. Wei, Y. L. Wu, Z. Zhang, G. H. Zhang, J. F. Duan, L. J. Li, H. L. Zhu, Z. Y. Zhu and Z. Y. Chen, *J. Alloys Compd.*, 2019, **778**, 731.

54 H. G. Li, S. B. Wang, M. J. Feng, J. P. Yang and B. M. Zhang, *J. Mater. Sci.*, 2018, **53**, 11607.

55 P. Wu, X. L. Xu, Q. Y. Zhu, X. S. Zhu, Y. W. Tang, Y. M. Zhou and T. H. Lu, *J. Alloys Compd.*, 2015, **626**, 234.